The Astrophysical Journal, 981:123 (11pp), 2025 March 10 https://doi.org/10.3847/1538-4357/adafa2

On Gamma Rays as Predictors of Ultra-high-energy Cosmic-Ray Flux in Active Galactic Nuclei

Cainã de Oliveira[1,3], Rodrigo Guedes Lang[2], and Pedro Batista[2]

[1] Instituto de Física de São Carlos, Universidade de São Paulo, Av. Trabalhador São-carlense 400, São Carlos, Brazil; caina.oliveira@usp.br

[2] Friedrich-Alexander-Universität Erlangen-Nürnberg, Erlangen Centre for Astroparticle Physics, Nikolaus-Fiebiger-Str. 2, 91058 Erlangen, Germany; rodrigo.lang@fau.de, pedro.batista@fau.de

Received 2024 August 12; revised 2025 January 27; accepted 2025 January 27; published 2025 March 4

Abstract

Active galactic nuclei (AGN) are among the main candidates for ultra-high-energy cosmic-ray (UHECR) sources. However, while some theoretical and phenomenological works favor AGNs as the main sources, recent works have shown that using the very-high-energy γ-ray flux as a proxy for the UHECR flux leads to a bad agreement with data. In this context, the energy spectrum and composition data are hardly fitted. At the same time, the arrival directions map is badly described and a spurious dipole direction is produced. In this work, we propose a possible solution to these contradictions. Using the observed γ-ray flux as a proxy may carry the implicit assumption of beamed UHECR emission and, consequently, its beam will remain collimated up to its detection on Earth. We show that assuming an isotropic UHECR emission and correcting the γ-ray emission proxy by Doppler boosting can overcome the problem. The combined fit of the spectrum and composition is improved, with a change of reduced χ^2 from 4.6 to 3.1. In particular, the tension between the observed and modeled dipole directions can be reduced from 5.9 (2.1)σ away from the data to 3.5 (1.1)σ for $E > 8$ EeV ($E > 32$ EeV). We also show that this effect is particularly important when including AGNs of different classes in the same analysis, such as radio galaxies and blazars.

Unified Astronomy Thesaurus concepts: Ultra-high-energy cosmic radiation (1733); Active galactic nuclei (16); Gamma-rays (637); Cosmic ray sources (328)

1. Introduction

The first detection of ultra-high-energy cosmic rays (UHECRs; J. Linsley 1963) raised significant questions about their origin. The discovery of astrophysical objects responsible for the acceleration of particles to ultra-high energies remains one of the most compelling mysteries in contemporary science (K. Kotera & A. V. Olinto 2011; R. Alves Batista et al. 2019). The small flux of UHECRs requires experiments with a very large area, up to thousands of square kilometers, to improve the detection of events and minimize experimental uncertainties (M. Nagano & A. A. Watson 2000). The Pierre Auger Observatory (The Pierre Auger Collaboration 2015) and Telescope Array (T. Abu-Zayyad et al. 2012) are the best examples of such feat with unprecedented exposure, leading to large statistics of high-quality data that allow precision studies in the ultra-high-energy range.

UHECR arrival direction measurements have been extensively used in the search for UHECR accelerators. On the large-scale anisotropies, one of the most significant results comes in the form of the dipole measured by the Pierre Auger Observatory. The measured dipole reaches 6.8σ confidence level (CL) for events with energies exceeding 8 EeV and points outward from the Galactic center at $\alpha = (97 \pm 8)^\circ$, $\delta = (-38^{+9}_{-9})^\circ$, which is powerful evidence for the dominance of extragalactic UHECR above this energy (A. Abdul Halim et al. 2024). For smaller-scale anisotropies, P. Abreu et al. (2022) reported a correlation between the arrival direction data of events with energies greater than 39 EeV and a jetted active galactic nuclei (AGN) catalog with a confidence of 3.3σ. The same analysis performed with a starburst galaxy (SBG) catalog reached 4.2σ CL. Combining Pierre Auger and Telescope Array data, a full-sky search for sources showed a correlation of 4.7σ (>38/49 EeV for Auger/Telescope Array) with the SBG catalog (A. di Matteo et al. 2023).

To consider particle physics processes and cosmic magnetic field deflections involved during the travel from the source to Earth, Monte Carlo simulations have been developed (R. Alves Batista et al. 2016; R. Aloisio et al. 2017). The results of numerical propagation are compared with observations, and the free parameters of the model (nuclei fraction, spectral index, maximum energy, spectrum normalization) are constrained by fitting the simulation results to experimental data (see, e.g., A. Aab et al. 2017; B. Eichmann et al. 2022; A. Abdul Halim et al. 2024).

Although the acceleration mechanism is generally assumed to be identical for a given class of objects (i.e., assuming identical spectral index), different approaches have been used to predict the UHECR luminosity of each object (A. Aab et al. 2018; B. Eichmann et al. 2018; B. Eichmann 2019; B. Eichmann et al. 2022; P. Abreu et al. 2022; C. de Oliveira & V. de Souza 2022, 2023; A. Abdul Halim et al. 2024; A. Partenheimer et al. 2024).

Several works have investigated AGNs as possible sources of UHECR. In radio galaxy scenarios, assuming the cosmic-ray flux is proportional to the jet power, it is possible to phenomenologically explain some characteristics of the spectrum, composition, and arrival direction (B. Eichmann et al. 2018; B. Eichmann 2019; B. Eichmann et al. 2022; C. de Oliveira & V. de Souza 2022). In particular, if Centaurus A (Cen A), M87, and Fornax A (For A) are considered

---

[3] Corresponding author.

dominant sources, the high-energy dipole and small-scale anisotropies can be explained (C. de Oliveira & V. de Souza 2022, 2023). In the unified model for AGNs, radio galaxies are blazars whose jets are misaligned with our line of sight. If radio galaxies are sources of UHECRs, it is reasonable to assume blazars are too. When the γ-ray luminosity (L_γ) is used as a proxy for the UHECR luminosity ($L_{\rm CR}$) in an AGN catalog, the data are hardly fitted (A. Abdul Halim et al. 2024; A. Partenheimer et al. 2024). In this case, the main issue is that the strong signal from the jetted AGN Mkn 421 ($\sim$130 Mpc) generates a hotspot not observed in the data and dominates the dipole direction. In addition, the fit to the spectrum is worsened by the high contribution of distant sources.

In this work, we propose a possible way to conciliate these two views by reviewing the motivations behind using L_γ as a proxy for $L_{\rm CR}$. In Section 2, we present a comparison of the theoretical predictions for the acceleration of UHECRs in AGN jets and the origin of the γ-ray radiation. We demonstrate that L_γ should be used carefully when applied as a weight to the UHECR flux. In Section 3, it is shown that, when considering the intrinsic γ-ray luminosity rather than the observed γ-ray luminosity, the combined fit of the spectrum and composition data improves, while the agreement between the predicted arrival directions and data is also enhanced. The main results and outlook of this work are summarized in Section 4.

2. Reviewing γ-Rays and Cosmic Rays in Jets

The deflections suffered by cosmic rays during their trajectory from the accelerator to the detection prevent the direct identification of their sources. Without reliable models of the extragalactic and Galactic magnetic fields, theoretical arguments are combined with constraints of cosmic magnetic fields in the source search. The usual approach to investigating possible individual sources focuses on the so-called local sources, with distances of $\lesssim$100 Mpc, for which the emitted UHECR will not have been as diffused as for farther sources and which may still maintain some information about the source location (R. G. Lang et al. 2021). It is common to consider every source as a standard candle with an effective spectral index but with different cosmic-ray luminosities, $L_{\rm CR}$. The observed luminosity in γ-rays, $L_\gamma^{\rm obs}$, has previously been used as a possible proxy (A. Aab et al. 2018; R. U. Abbasi et al. 2018; P. Abreu et al. 2022; A. Abdul Halim et al. 2023; A. Abdul Halim et al. 2024; A. Partenheimer et al. 2024). However, a bad agreement between the model for AGNs and data is found with this assumption, in particular due to a strong contribution from Mkn 421, a blazar located at $\sim$130 Mpc. In this section, we explore the assumption of using $L_\gamma^{\rm obs}$ as a proxy for $L_{\rm CR}$ in AGNs and argue that the intrinsic luminosity $L_\gamma^{\rm int}$ may be a more robust assumption.

The A. M. Hillas (1984) condition is the minimum requirement when considering astrophysical objects as possible accelerators. The lobes, knots, and hotspots of jetted AGNs satisfy the Hillas condition for acceleration up to the ultra-high-energy scale (R. Alves Batista et al. 2019). AGNs have been considered prime UHECR source candidates in different contexts (S. S. Kimura et al. 2018; J. H. Matthews et al. 2018a; B. Eichmann et al. 2018; B. Eichmann 2019; B. Eichmann et al. 2022; C. de Oliveira & V. de Souza 2022; F. M. Rieger 2022; C. de Oliveira & V. de Souza 2023), in particular due to the UHECR hotspot detected at 4σ by the Pierre Auger Observatory around the direction of Cen A (A. Abdul Halim et al. 2023).

Several sites in the structure of an AGN have been proposed as suitable for particle acceleration (see J. H. Matthews et al. 2020; F. M. Rieger 2022 for reviews), e.g., the neighborhood of the supermassive black hole (G. Katsoulakos & F. M. Rieger 2018; C. H. Coimbra-Araújo & Q. Anjos 2020; C. H. Coimbra-Arajo & R. C. dos Anjos 2022), parsec- and kiloparsec-scale jets (S. S. Kimura et al. 2018; X. Rodrigues et al. 2018; J. Seo et al. 2023, 2024), backflow of the jet material (J. H. Matthews et al. 2018a), the termination shock (B. Cerutti & G. Giacinti 2023), and the lobes (S. O'Sullivan et al. 2009).

2.1. γ-Rays in Jets

The broadband spectral energy distribution of jetted AGNs has been measured from radio to γ-rays, with a characteristic double-peaked shape. The detection of X-ray and γ-rays demonstrated the existence of regions of particle acceleration along AGNs' jets (e.g., R. Blandford et al. 2019). The lower-energy peak is normally attributed to synchrotron radiation from the interaction between accelerated electrons and positrons and the magnetic fields of the medium (e.g., C. D. Dermer & G. Menon 2009). As for the higher-energy peak, the most common hypotheses rely on the upscattering of low-energy photons to γ-ray energies, by higher-energy leptons, via inverse Compton (IC) processes (e.g., J. D. Finke et al. 2008). These low-energy photons can originate from the synchrotron radiation emitted by the same particle population, known as synchrotron self-Compton emission, or from thermal radiation coming from the broad and narrow-line regions, the accretion disk, and the torus, known as external Compton emission (e.g., M. Böttcher et al. 2013).

The acceleration of hadrons also must occur at least as efficiently as electrons (e.g., A. Atoyan & C. Dermer 2004). Radiation of hadronic origin, mainly from pion decays, may be added to the leptonic emission. Both proton–photon and proton–proton interactions can be responsible for γ-ray creation via neutral pion decay and successive electromagnetic cascades. In general, γ-rays from pion decay carry approximately 10% of the energy of one high-energy proton. Due to the increased number of intermediate reactions, γ-rays originating from charged pions require higher proton energies. Then, the detection of γ-rays in the TeV scale can imply the existence of protons with energy in the PeV scale (S. R. Kelner et al. 2006; M. Böttcher 2012; G. Cao & J. Wang 2014).

It is important to note that for increasing γ-ray energies (starting at TeV), absorption via interactions with extragalactic background light (EBL) and cosmic microwave background (CMB) photons are more likely to occur, which greatly reduces the flux of γ-rays above such energies on Earth (A. De Angelis et al. 2013; L. Gréaux et al. 2024).

The most common geometry of jet emission models consists of particles being accelerated in a compact region that is traveling at relativistic speeds down the jet. In this region, also known as the *blob*, the plasma of particles moves with a bulk Lorentz factor Γ_b along the jet axis, while emitting photons isotropically in the blob's rest frame. For highly relativistic motions ($\Gamma_b \gg 1$), an isotropic emission in the blob's comoving frame will be observed on Earth as a beamed emission, with a beaming angle $\theta_{\rm beam} = \Gamma_b^{-1}$ (C. D. Dermer & G. Menon 2009).

Relativistic transformations of the photon energy and emission angle will impact the observed photon flux. The intrinsic and observed energy of a photon, $\epsilon_\gamma^{\rm int}$ and $\epsilon_\gamma^{\rm obs}$, respectively, are related by the Doppler factor $\mathcal{D}$, defined as $\mathcal{D} \equiv \frac{\epsilon_\gamma^{\rm obs}}{\epsilon_\gamma^{\rm int}} = [\Gamma_b(1 - \beta_b\cos\theta)]^{-1}$, where β_b is the normalized velocity of the blob, and θ is the angle between the jet axis and Earth's line of sight.

The observed photon flux is related to the intrinsic photon flux of a source, but is subject to relativistic transformations, being strongly dependent on the Doppler factor. The ratio between the observed flux density $F_\gamma^{\rm obs}$ of photons on Earth and the intrinsic photon flux density $F_\gamma^{\rm int}$ is

$$\frac{F_\gamma^{\rm obs}}{F_\gamma^{\rm int}} = \frac{\nu_\gamma^{\rm obs}}{\nu_\gamma^{\rm int}}\frac{d\nu_\gamma^{\rm int}}{d\nu_\gamma^{\rm obs}}\frac{dN_\gamma^{\rm obs}}{dN_\gamma^{\rm int}}\frac{dt_\gamma^{\rm int}}{dt_\gamma^{\rm obs}}\frac{d\Omega_\gamma^{\rm int}}{d\Omega_\gamma^{\rm int}}, \tag{1}$$

where $d\Omega = dA/d_L^2$, and d_L^2 is the invariant luminosity distance. From Equation (1), it is possible to show that the observed flux of photons at Earth, $\Phi_\gamma^{\rm obs}$, and therefore the observed luminosity $L_\gamma^{\rm obs}$, is boosted by a factor $\mathcal{D}^4$ in relation to the intrinsic luminosity $L_\gamma^{\rm int}$, $L_\gamma^{\rm obs} = \mathcal{D}^4 L_\gamma^{\rm int}$ (M. Böttcher 2012).

2.2. UHECR Acceleration in AGNs

UHECRs should be accelerated along the jet by different mechanisms in different regions (S. S. Kimura et al. 2018; J. H. Matthews et al. 2020; F. M. Rieger 2022; J. Seo et al. 2023, 2024). Magnetic reconnection can be present at the highly magnetized jet base (T. E. Medina-Torrejón et al. 2021). Diffusive shock acceleration should dominate in the shocked regions of the jet beam, backflow, and termination shock. Shear acceleration can occur in regions of high-velocity gradients, caused by the highly relativistic jet, and even in the neighborhood of the termination shock (B. Cerutti & G. Giacinti 2023). Acceleration by second-order Fermi acceleration is possible in turbulent regions of the lobes. Only UHECRs accelerated in the relativistic beamed plasma is subject to the beaming effect.

UHECRs could be accelerated in shocks present in the jet. (X. Rodrigues et al. 2018; B. T. Zhang & K. Murase 2023; A. Zech & M. Lemoine 2021). In general, highly relativistic shocks are not efficient UHECR accelerators, and mildly relativistic shocks are more promising (M. Lemoine & G. Pelletier 2010; B. Reville & A. R. Bell 2014; A. R. Bell et al. 2017; J. H. Matthews et al. 2018a). The cosmic-ray emission must be isotropic in the shock rest frame, so relativistic beaming is expected in the laboratory rest frame. The shocks should accelerate not only cosmic rays but also electrons, which will radiate downstream of the shock, where the plasma Doppler factor will modulate the emission, as discussed in the previous section (e.g., A. Zech & M. Lemoine 2021). Even in mildly relativistic jets, the flux corrections due to the Doppler factor can be significant, since the observed luminosity depends on $\mathcal{D}^4 = \left(\frac{1+\beta}{1-\beta}\right)^2 \sim 3$–80, for $\beta \sim 0.5$–0.8 and line-of-sight jets. However, the angular distribution of the UHECR is likely to be isotropized (in the laboratory frame) within the source region since these particles will cross the magnetized jet and the lobes before escaping, both with complex magnetic field structures, and with the jet itself being subject to turbulences and the presence of knots (J. L. Goodger et al. 2009; R. P. Dubey et al. 2023; G. Mattia et al. 2023).

Consider the propagation and possible acceleration of an UHECR along a kiloparsec-scale jet. Combining hydrodynamics and Monte Carlo simulations, J. Seo et al. (2023, 2024) found that the main mechanism accelerating the UHECR above a few EeV is the relativistic shear acceleration at the interface jet–backflow. Combining magnetohydrodynamics with particle-in-cell simulations, G. Mattia & D. Caprioli (2019) made a detailed study of the angular distribution of UHECR emission on a kiloparsec-scale jet. The angular distribution of the accelerated UHECR depends mainly on the toroidal component of the jet magnetic field that can disperse (isotropic emission) or collimate (anisotropic emission) particles. The direction of emission will also be determined by the deflections inside the cocoon.[4] In an anisotropic scenario, only about half of the particles were collimated inside an angle larger than $\Gamma_{\rm jet}^{-1}$.

As an AGN's jet inflates the lobes (R. Morganti 2017; M. J. Hardcastle & M. G. H. Krause 2014; R. J. Turner et al. 2022), the UHECR beam should cross them before reaching the extragalactic medium. Due to its extension and the presence of turbulent/filamentary magnetic field (C. Carilli & P. Barthel 1996; F. Massaro & M. Ajello 2011; D. Guidetti et al. 2011; M. J. Hardcastle & M. G. H. Krause 2014; S. Wykes et al. 2014, 2015; X.-n. Sun et al. 2016; L. A. L. Andati et al. 2024), it is likely that the UHECR scatters inside the lobes, losing its directional information. The scattering length of a UHECR can be approximated as (S. O'Sullivan et al. 2009; R. G. Lang et al. 2020)

$$\lambda_{\rm scatt} \sim \kappa^2 \ell_c \left(\frac{r_L}{\ell_c}\right)^\delta, \tag{2}$$

where $\kappa^2 = B_0^2/\delta B^2$, ℓ_c is the acoherence length of the magnetic field, δ is the diffusion coefficient, and

$$r_L \approx \frac{E/\mathrm{EeV}}{Z}\frac{1\quad \mathrm{kpc}}{B_0/\mu\mathrm{G}} \tag{3}$$

is the gyroradius of the UHECR of charge Z. B_0 and δB are the large-scale and turbulent components of the magnetic field, respectively.

The lobes extend across $R \sim 100$ kpc with magnetic fields ~1–10 μG (F. Massaro & M. Ajello 2011; S. Wykes et al. 2015; M. J. Hardcastle et al. 2015; X.-n. Sun et al. 2016; L. A. L. Andati et al. 2024). The coherence length of the magnetic field is assumed to be $\ell_c \sim 0.1 \times R \sim 10$ kpc (B. Adebahr et al. 2019; S. O'Sullivan et al. 2009). If $\lambda_{\rm scatt}$ is smaller than R, the UHECR will suffer at least one episode of scattering inside the lobes, losing its directional information. The major energy dissipation of the jet occurs in the ~parsec scale from the jet base (A. L. W. Harvey et al. 2020; A. Shukla & K. Mannheim 2020). Then, considering $\lambda_{\rm scatt} \sim R$, we get the energy threshold for one scattering:

$$E_{\rm scatt} \sim (Z \times 10\quad \mathrm{EeV})\,\ell_{10} B_{\mu G}\left(\frac{10 R_{100}}{\ell_{10}\kappa^2}\right)^{1/\delta}, \tag{4}$$

where $\ell_{10} = \ell/10\,\mathrm{kpc}$, $R_{100} = R/100\,\mathrm{kpc}$, and $B_{\mu G} = B_0/\mu\mathrm{G}$. In a conservative estimation, we consider the high-energy nonresonant regime, $\delta = 2$ (N. Globus et al. 2008), and the fiducial value $\kappa \approx 1$ ($B_0 \sim \delta B$) (S. O'Sullivan et al. 2009;

---

[4] A region of shocked material surrounding the jet (e.g., M. C. Begelman & D. F. Cioffi 1989).

S. Wykes et al. 2014):

$$E_{\mathrm{scatt}} \sim (Z \times 30\,\mathrm{EeV})\,\delta B_{\mu G}\sqrt{\ell_{10} R_{100}}\,. \tag{5}$$

Even if accelerated in relativistic blobs inside the jet, protons with energies up to ~30 EeV will lose their directional information in the source by being isotropized while traveling through the lobes. However, due to limitations in the acceleration capacity of the sources, UHECRs are unlikely protons up to such high energies. Assuming an electromagnetic origin for the UHECR acceleration, it is useful to introduce the magnetic rigidity $R = E/Z$. The combined fit performed by the Pierre Auger Collaboration (A. Abdul Halim et al. 2024) indicates a magnetic rigidity cutoff $R_{\mathrm{cut}} \lesssim 10$ EV at the sources, and the flux at Earth being dominated by He and N above the ankle (5 EeV), with successive heavier compositions. Taking $Z \sim 5$, we get $E_{\mathrm{scatt}} \sim 150$ EeV, encompassing most of the detected UHECRs. This value can still be larger since photodisintegration makes the composition lighter after propagation from the source.

This estimation depends on the position of the accelerator in the jet. The scattering can be inefficient if the acceleration occurs mainly on the termination shocks, observed as the hotspot found in FR II radio galaxies (M. J. Hardcastle et al. 2007; B. Snios et al. 2020). As relativistic shocks, the termination shocks are poor accelerators of UHECRs (A. T. Araudo et al. 2017). Yet, recently B. Cerutti & G. Giacinti (2023) found that particles can be efficiently accelerated up to $\sim 10^{20}$ eV by crossing a cavity behind the termination shock. In this case it is unclear if a possible beamed emission will be sustained after leaving the acceleration region. The magnetic field of the vortex downstream of the cavity or of the hotspot itself might decollimate the beam, at least partially.

3. Implications for the Search for Sources

If particle acceleration occurs in the jet of an AGN, it is reasonable to assume that a fraction of the jet kinetic power will be converted into UHECR kinetic energy (B. Eichmann et al. 2018; B. Eichmann 2019; J. H. Matthews & A. M. Taylor 2021). The intrinsic γ-ray luminosity is significantly correlated with the jet power of an AGN from different categories (R. S. Nemmen et al. 2012; Y. Chen et al. 2023a). In addition, γ-ray emission is linked to particle acceleration and interactions in its neighborhoods (e.g., B. Reville & A. R. Bell 2014; B. T. Zhang & K. Murase 2023). In this way, using γ-ray luminosity as a possible normalization for the UHECR flux from different sources is well justified. Nevertheless, when considering the γ-rays emitted from particles accelerated in relativistic blobs moving along the jet, the γ-ray flux suffers a Doppler boost in the jet direction, while the same is unlikely for UHECR emission.

In this section, we explore the implications of using the observed and intrinsic γ-ray luminosity of sources as a proxy for the UHECR luminosity. As a case study, we use the γAGN catalog selected from the analysis of the Pierre Auger Collaboration (A. Abdul Halim et al. 2024). The selection contains jetted AGNs measured with the Fermi-LAT with a γ-ray flux $>3.3 \times 10^{-11}\mathrm{cm}^{-2}\mathrm{s}^{-1}$ between 10 GeV and 1 TeV from the Fermi 3FHL catalog (M. Ajello et al. 2017). The determination of $\mathcal{D}$ is described in the Appendix, and the relevant properties are given in Table 2.

3.1. γ-Ray Luminosity as a Proxy for UHECR Luminosity

Assuming that the UHECR emission scales with the intrinsic characteristics of the source but it is not beamed, the use of L_γ^{obs} as a proxy for L_{CR} may overestimate the UHECR luminosity by a factor $\sim\mathcal{D}^q$, where q takes into account the different proxies between γ-rays and UHECR. The beaming effect becomes especially important when different classes of AGNs are included in the same analysis, such as radio galaxies and blazars. Due to the viewing angle, radio galaxies (RG) have a mean Doppler factor $\mathcal{D}_{\mathrm{RG}} \sim 2.6$ (X.-H. Ye et al. 2023), while for BL Lacs (BLL), $\mathcal{D}_{\mathrm{BLL}} \sim 10$ (L. Zhang et al. 2020; X.-H. Ye et al. 2023). Two scenarios are studied, both assuming an isotropic emission of UHECRs. First, the UHECR luminosity is assumed proportional to the intrinsic γ-ray luminosity of the source, and then the usual bolometric correction $q = 4$ applies. Second, the UHECR luminosity is considered to be dependent directly on the radiative jet power, and then $q = 2$ (L. Maraschi & F. Tavecchio 2003; Y. Chen et al. 2023b; R. S. Nemmen et al. 2012).[5] Since the observed luminosity is proportional to $\mathcal{D}^q$, this overestimates the UHECR flux from BL Lacs when compared to radio galaxies on average by a factor of $(\mathcal{D}_{\mathrm{BLL}}/\mathcal{D}_{\mathrm{RG}})^q \sim 15$–200.

Figure 1 shows the different luminosity weights used as proxies for the UHECR luminosity. The circle area represents the expected flux on Earth and is linearly proportional to the luminosity of each source. Sources with L_{CR} smaller than 1% of the largest value in each panel are shown as black diamonds of fixed size. When comparing panels (a) with (b) and (c), the importance of considering the beaming effect in the γ-ray luminosity of each source is made clear. Even though Mkn 421 is the dominant source using L_γ^{obs} (case a), it becomes negligible in any scenario where Doppler boosting effects are considered (cases b and c). In cases where the intrinsic source characteristics are considered (cases b and c), the radio galaxies Cen A, M87, and For A are the brightest sources in the field of view of the Pierre Auger Observatory. Considering the entire sky, the distant ($\sim$200 Mpc) blazars Mkn 180 can dominate over the nearby radio galaxies. This blazar presents a small Doppler factor ($\sim$1.4) when compared to the others BL Lacs in the sample. Note that the strong dependence on $\mathcal{D}$ makes the estimation of the flux very sensitive to its uncertainties: Comparing the γ-ray flux from Cen A and Mkn 180, a Doppler factor $\mathcal{D}_{\mathrm{Mkn180}} \sim (F_{\mathrm{3fhl}}^{\mathrm{Mkn180}}/F_{\mathrm{3fhl}}^{\mathrm{CenA}})^{1/q} \sim 1.2 - 1.4$ is enough to make the UHECR luminosity of Mkn 180 equal to that from Cen A.

3.2. Results from the Combined Fit

The proxies for the cosmic-ray luminosity only provide an estimation of the emissivities of each source considered. UHECRs undergo different energy- and primary-dependent energy losses during propagation, which modulate the final spectrum and composition. For that reason, the final contribution from each source will strongly rely on the astrophysical model assumed for the sources, i.e., their injected spectra and compositions. To take this into account, we performed a combined spectrum and composition fit, following the approach of previous works by the Pierre Auger Collaboration (A. Aab et al. 2017; A. Abdul Halim et al. 2024). One-dimensional simulations in `CRPropa3` (R. Alves Batista et al.

---

[5] This value is valid for $\mathcal{D} \approx \Gamma$.

2016) were performed in a uniform grid of energy (from 10^{18} eV to 10^{22} eV with 10 bins per decade), and distance (from 3 to 3342 Mpc in 118 bins in log) for each of the five representative primaries, ^{1}H, ^{4}He, ^{14}N, ^{28}Si, and ^{56}Fe. All the energy losses and the EBL model of R. C. Gilmore et al. (2012) were considered. A smearing was introduced in the arrival directions via a von Mises–Fisher distribution (R. Fisher 1953) similar to that of A. Abdul Halim et al. (2024, Equation 2.14), with $\Delta_0 = 5^\circ$ and $R_0 = 10$ EV. The direction-dependent exposure of the experiment was taken into account to consider only events with zenith angles smaller than 60°. The effective spectrum of each source was fitted to

$$dN/dE(E) = \begin{cases} N_s F_i E^{-\Gamma}, & \text{for } E \leqslant Z_i \mathrm{R}_{\max} \\ N_s F_i E^{-\Gamma} e^{(1-E/(Z_i R_{\max}))}, & \text{for } E > Z_i \mathrm{R}_{\max} \end{cases}, \tag{6}$$

where the free parameters of the fit are the spectral index, Γ, the maximum rigidity at the sources, $R_{\max}$, the main normalization, and the contribution of each species, F_i. F_i is defined as the total contribution of a primary between 1 EeV and the corresponding maximum energy, $ZR_{\max}$. This definition relates to that of A. Aab et al. (2017), f_i (i.e., the relative contribution of each primary for an energy bin below the maximum energy of protons) as $f_i = F_i/(Z_i R_{\max})^{(\Gamma-1)}$. Such quantity was chosen because it provides a more robust minimization procedure for the fit. The sources were divided into two classes: a homogeneous distribution of background sources with equal emissivity and no source evolution, and the so-called local sources, whose individual emissivities are modulated by the values in Table 2. The relative contribution of local and background sources is given by the parameter $\alpha = J_{\mathrm{local}}(E = 10^{19.5}\,\mathrm{eV})/J_{\mathrm{background}}(E = 10^{19.5}\,\mathrm{eV})$. Both the normalization for the background sources and α are also free parameters of the fit.

The simulations are multiplied by the weights described above and compared to the spectral data above $10^{18.7}$ eV from V. Verzi (2020) and measurements of the first and second moments of the $X_{\max}$ distributions from A. Yushkov (2020).[6] The fit was performed by minimizing the χ^2 distance between the model and the spectral/composition data.

The systematic uncertainties in the spectrum and $X_{\max}$ were addressed by performing a new fit with the data shifted by $\pm 14\%$ for the energy and $\pm 1\sigma$ for the $X_{\max}(E)$ according to A. Aab et al. (2014), resulting in a total of nine fits for each of the cases (a), (b), and (c). No shift in $X_{\max}$ was preferred by the fit for every case. For energy, on the other hand, the data were best described with $E \to E - 14\%$, $E \to E + 0\%$, and $E \to E + 14\%$ for L_γ^{obs}, $\mathcal{D}^{-2}L_\gamma^{\mathrm{obs}}$, and $\mathcal{D}^{-4}L_\gamma^{\mathrm{obs}}$, respectively. The $X_{\max}$ moments were related to the mass compositions using the EPOS-LHC hadronic model (T. Pierog et al. 2015). Different hadronic models were tested, but the hierarchy between the fit results for each proxy remained the same.

Figure 2 shows the spectrum and $X_{\max}$ moments for the best fit of the $\mathcal{D}^{-2}L_\gamma^{\mathrm{obs}}$ scenario. Similar to the previous results found by the Pierre Auger Collaboration in the absence of an extragalactic magnetic field, a very hard spectrum with $\Gamma < 0$ with a strict rigidity cutoff, $R_{\max} = 10^{18.11}$ V, is preferred.

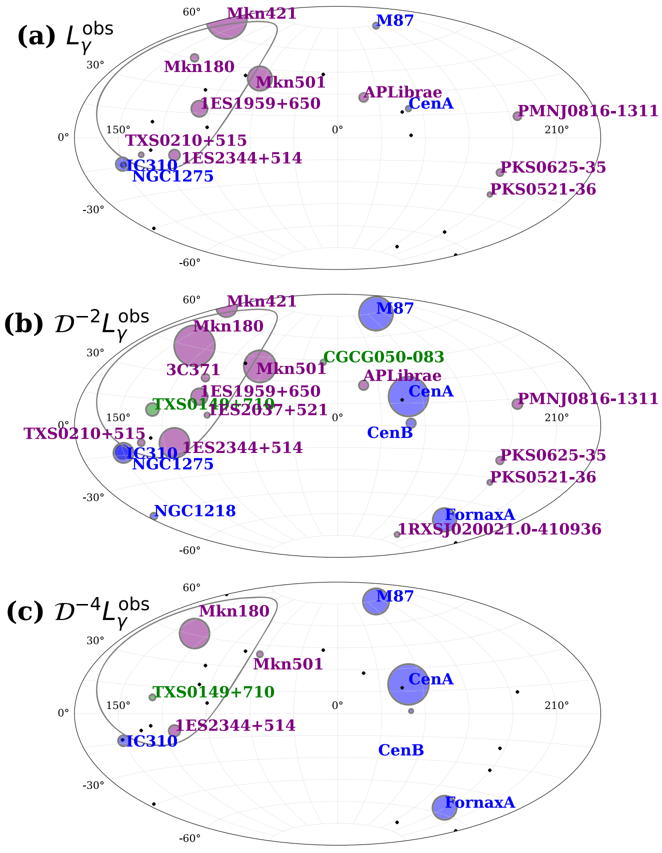

Figure 1. Luminosity weights used as a proxy for the UHECR flux of AGNs, using (a) the observed γ-ray flux, (b) $\mathcal{D}^{-2}L_\gamma^{\mathrm{obs}}$, and (c) $\mathcal{D}^{-4}L_\gamma^{\mathrm{obs}}$. The circle size is linearly proportional to the contribution of each source, normalized by the contribution of the brighter source in each panel. Sources with a contribution above 10^{-2} of the maximum contribution are shown as circles (blue = radio galaxies, green = blazar candidate of unknown origin, purple = BL Lacs). Other sources are represented by black diamonds.

The resulting goodness-of-fit values were $(\chi^2/\mathrm{NDF})_{L_\gamma^{\mathrm{obs}}} = 114.9/25 \approx 4.6$, $(\chi^2/\mathrm{NDF})_{\mathcal{D}^{-2}L_\gamma^{\mathrm{obs}}} = 77.6/25 \approx 3.1$, and $(\chi^2/\mathrm{NDF})_{\mathcal{D}^{-4}L_\gamma^{\mathrm{obs}}} = 98.6/25 \approx 3.9$, demonstrating an improvement of the fit when the new proposed proxies are considered, in particular the $\mathcal{D}^{-2}L_\gamma^{\mathrm{obs}}$ case. The main reason for this comes from the relative contribution of farther local sources. A larger contribution from a very local source such as Cen A will result in a total spectrum with a spectral index very similar to the intrinsic spectral index assumed for the sources. When larger relative contributions from farther sources are predicted, an effective spectral index is seen in the combined local source flux. This is mostly due to two effects: the suppression will occur at different energies for sources at different distances, and more UHECRs from farther sources will go through photodisintegration, resulting in a larger contribution to lower energies in the spectrum. This shapes the final spectrum on Earth and vastly increases the contribution of local sources to the lower-energy end of the spectrum, leading to a poor fit of the data.

The most important effect is seen in the distributions of arrival directions. Figure 3 shows the arrival direction maps for $E > 8$ EeV and $E > 32$ EeV. The counts for each of the 49,152 pixels with equal solid angle are normalized to the pixel with the fewest counts, such that pixels with only contribution from background sources are set to 1. An overall normalization is

---

[6] Taken from Pierre Auger's public data set: https://www.auger.org/science/public-data/data.

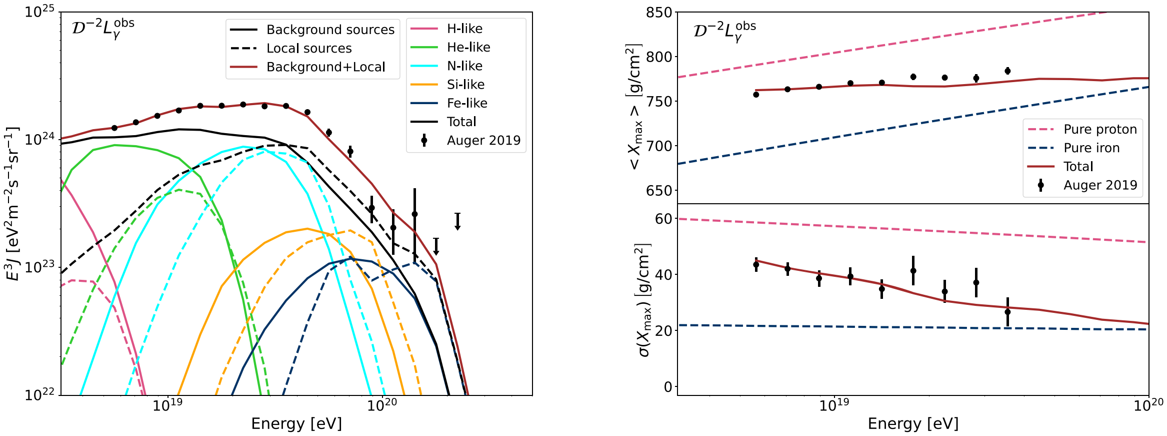

Figure 2. Spectrum (left) and first two moments of the $X_{\rm max}$ distribution (right) for the best-fit case scenario using $D^{-2}L_\gamma^{\rm obs}$ as a proxy. The full and dashed lines in the left panel show the contribution of background and local sources, respectively. The different masses arriving on Earth are grouped into H-like ($A = 1$), He-like ($2 \leqslant A \leqslant 4$), N-like ($5 \leqslant A \leqslant 22$), Si-like ($23 \leqslant A \leqslant 38$), and Fe-like ($39 \leqslant A \leqslant 56$), and are represented by the different colors. The dashed lines on the right panel show the expectations for an extreme pure composition scenario. The best-fit parameters are $\Gamma = -2.0^{+0.06}_{-0.61}$, $\log_{10}(R_{\rm max}/{\rm V}) = 18.11^{0.02}_{-0.04}$, and $\alpha = 49 \pm 1\%$. No systematic shift for energy or $X_{\rm max}$ is preferred.

arbitrary as it does not influence the structures of the map. A log scale is chosen to help highlight different hotspots. The reconstructed dipole directions for the full sky and field of view of the Pierre Auger Observatory are also shown for each case. Figure 4 shows the relative contribution of each local source to the spectrum for the same energy ranges.

The hotspots change for each scenario considered. The dominance of Mkn 421 seen in $L_\gamma^{\rm obs}$ vanishes for the new proxies. As seen in Figure 4, its contribution is suppressed by 2–5 orders of magnitude depending on the proxy and energy range. This source was reported in A. Abdul Halim et al. (2024) as the biggest challenge for performing a combined fit of the Pierre Auger Collaboration data using arrival direction, due to its relatively large distance, position within Auger's field of view, and predicted UHECR contribution, which was in contrast with data. This challenge seems to be overcome by the new proxies proposed in the work.

For both the $\mathcal{D}^{-2}L_\gamma^{\rm obs}$ and $\mathcal{D}^{-4}L_\gamma^{\rm obs}$ cases, the main hotspots are seen around Cen A, For A, M87 and a few sources outside Auger's field of view, in particular Mkn 180 and 1ES2344 +514. The lack of a hotspot near M87 in the data could be explained by a shadowing due to the effect of extragalactic and galactic magnetic fields (C. de Oliveira & V. de Souza 2022; A. Condorelli et al. 2023; C. de Oliveira & V. de Souza 2023). The remaining three hotspots are in relative agreement with the two hotspots reported by the Pierre Auger Observatory, $(\ell, b) \approx (310°, 20°)$ and $(\ell, b) \approx (270°, -75°)$ (A. Aab et al. 2018) and the hotspot reported by the Telescope Array Observatory, $(\alpha, \delta) = (144°, 40.5°)$, or, in galactic coordinates, $(\ell, b) = (181.5°, 47.8°)$ (J. Kim et al. 2023).

The reconstructed dipoles are also improved with the new proxy assumptions. The reconstructed amplitude for the $L_\gamma^{\rm obs}$ proxy and $E > 8$ EeV was $d = 14\% \pm 1\%$, too large when compared to the amplitude of $7.4^{+1.0}_{-0.8}\%$ reported by A. Abdul Halim et al. (2024). This again comes from an overcontribution of Mkn 421. For the new proxies, $\mathcal{D}^{-2}L_\gamma^{\rm obs}$ and $\mathcal{D}^{-4}L_\gamma^{\rm obs}$, the suppression of Mkn 421 leads to smaller reconstructed amplitudes of $d = 7.5\% \pm 0.2\%$ and $d = 4.1\% \pm 0.5\%$. Higher-order multipoles are not investigated in this work, as they are significantly more susceptible to diffusion in the galactic and extragalactic magnetic fields, neglected in this work (C. A. de Oliveira et al. 2024).

Improvements can also be seen in the reconstructed direction of the dipole. As seen in Figure 3, none of the reconstructed dipole directions agree within 1σ with the experimental data. Nevertheless, for the Auger dipole, the tension between the directions of the observed and modeled dipoles is reduced with the new proxies. We calculate the angular distance between the reconstructed and measured dipole and compare that to the 1σ uncertainty in the measurement, and show that for the field of view of Auger an improvement from 5.9 (2.1)σ to 3.5 (1.1)σ is found for $E > 8(32)$ EeV. The results for both Auger's field of view and full sky are shown in Table 1. Nevertheless, it is worth pointing out that the spectral and composition fit were done considering only Auger data. Different results would be expected if data from Auger and the Telescope Array were combined, as is the case for the full-sky measurements.

4. Summary and Discussion

AGNs are among the main candidates responsible for the acceleration of cosmic rays up to 10^{20} eV. Different views on the relative contribution from each source have been explored in previous works, leading to a significant change in the agreement with data. In this work, we reconcile these studies with a thorough investigation of the γ-ray luminosity proxy for UHECRs.

1. *The association between γ-rays and UHECRs is weak, but not impossible.* γ-rays can have an origin in leptonic or hadronic scenarios. In the hadronic case, the cosmic-ray energy necessary to produce a ~TeV γ-ray is ~PeV, considerably below the UHECR regime. γ-rays emitted by EeV UHECRs will likely have energies not accessible by γ-ray observatories due to EBL and CMB attenuation. In this way, the correlation between γ-rays and UHECRs can be considered weak, although it should not be ignored, since the detection of γ-ray radiation implies the existence of regions where the acceleration of charged particles occurs. Furthermore, the γ-ray luminosity is

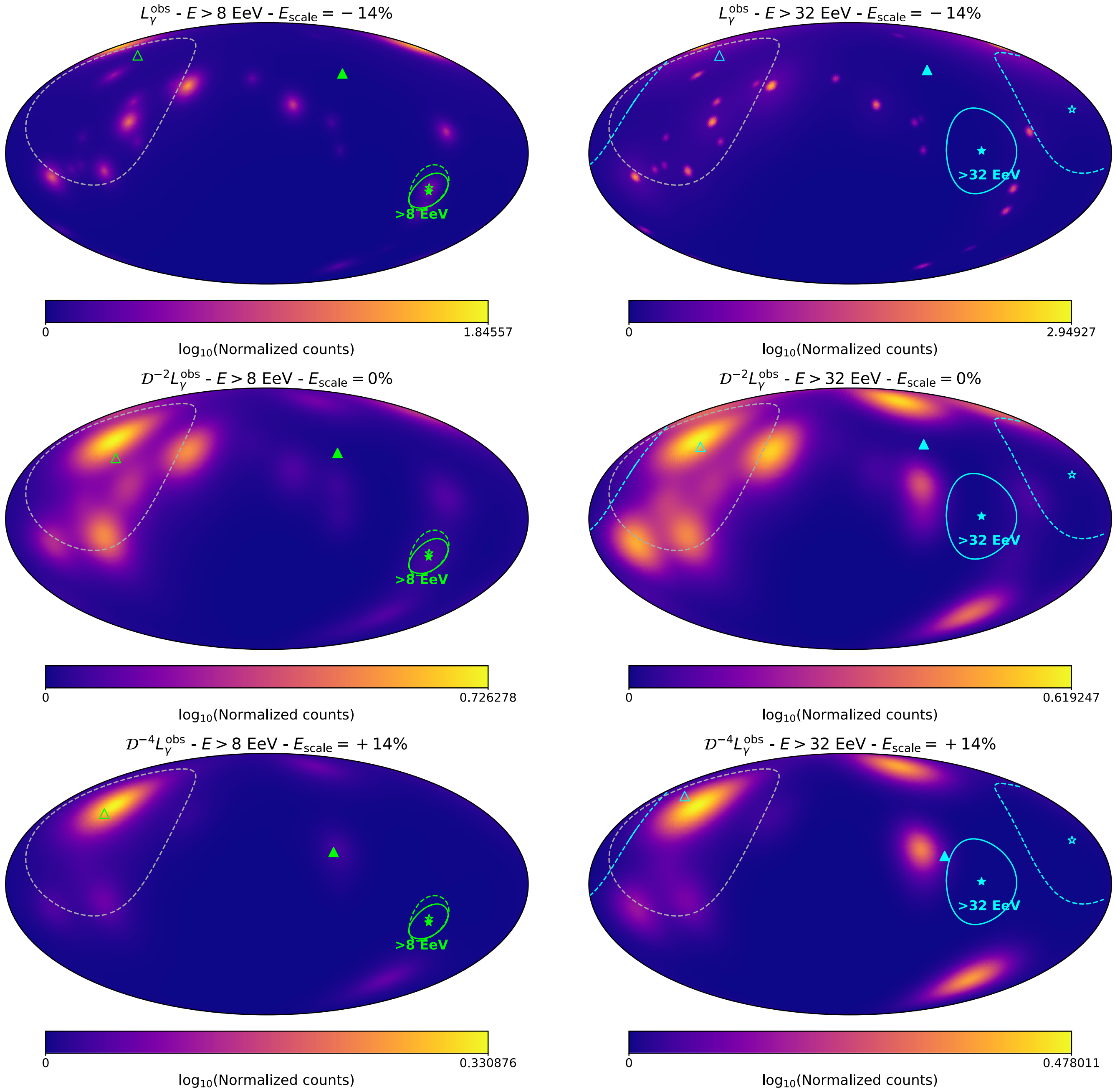

Figure 3. Arrival direction maps. Each row shows the results from the best-fit scenario considering each of the γ-ray proxies, and the left and right columns show the result for $E > 8$ EeV and $E > 32$ EeV, respectively. The counts are normalized to the bin with the fewest counts, i.e., regions that have negligible contribution from local sources. The lime and cyan full stars and contours show the dipole measured by the Pierre Auger Observatory for $E > 8$ eV and $E > 32$ eV, while the lime and cyan empty stars and dashed contours show the full-sky dipole measured by a combined analysis of the Pierre Auger Observatory and Telescope Array (A. Abdul Halim et al. 2023). Open and closed triangles show the obtained dipoles for the full sky and just for the Auger field of view for our scenarios, respectively. The dashed gray contour shows Auger's field of view considering events with zenith angles smaller than 80°. A rigidity-dependent blurring, following a von Mises–Fisher distribution (A. Abdul Halim et al. 2024, Equation 2.14) with $\Delta_0 = 5^\circ$ and $R_0 = 10$ EV, was used for the local sources.

related to the jet power in an AGN, which can be related to its UHECR luminosity.

2. *The use of the observed flux of γ-rays as proxies for UHECRs implicitly assumes that both are beamed.* When the γ-ray flux is used as a proxy for the UHECR flux, there is an implicit hypothesis that UHECRs are subject to the same beaming effect as γ-rays. It is unclear if UHECRs are accelerated in relativistic blobs as is assumed for γ-rays. However, even in that case, the magnetic fields in the acceleration regions, jets, and lobes will likely decollimate the UHECR beam, as shown in numerical studies. In this way, the expected emission cone of UHECRs is larger than that of γ-rays.
3. *The correction of the observed flux of γ-rays as proxies for UHECR is source dependent and on average decreases the contribution for farther sources.* Assuming that UHECRs are not beamed as γ-rays, the intrinsic γ-ray luminosity or the radiative jet power are better proxies than the observed γ-ray luminosity. The relation between them with the observed γ-ray luminosity is given by

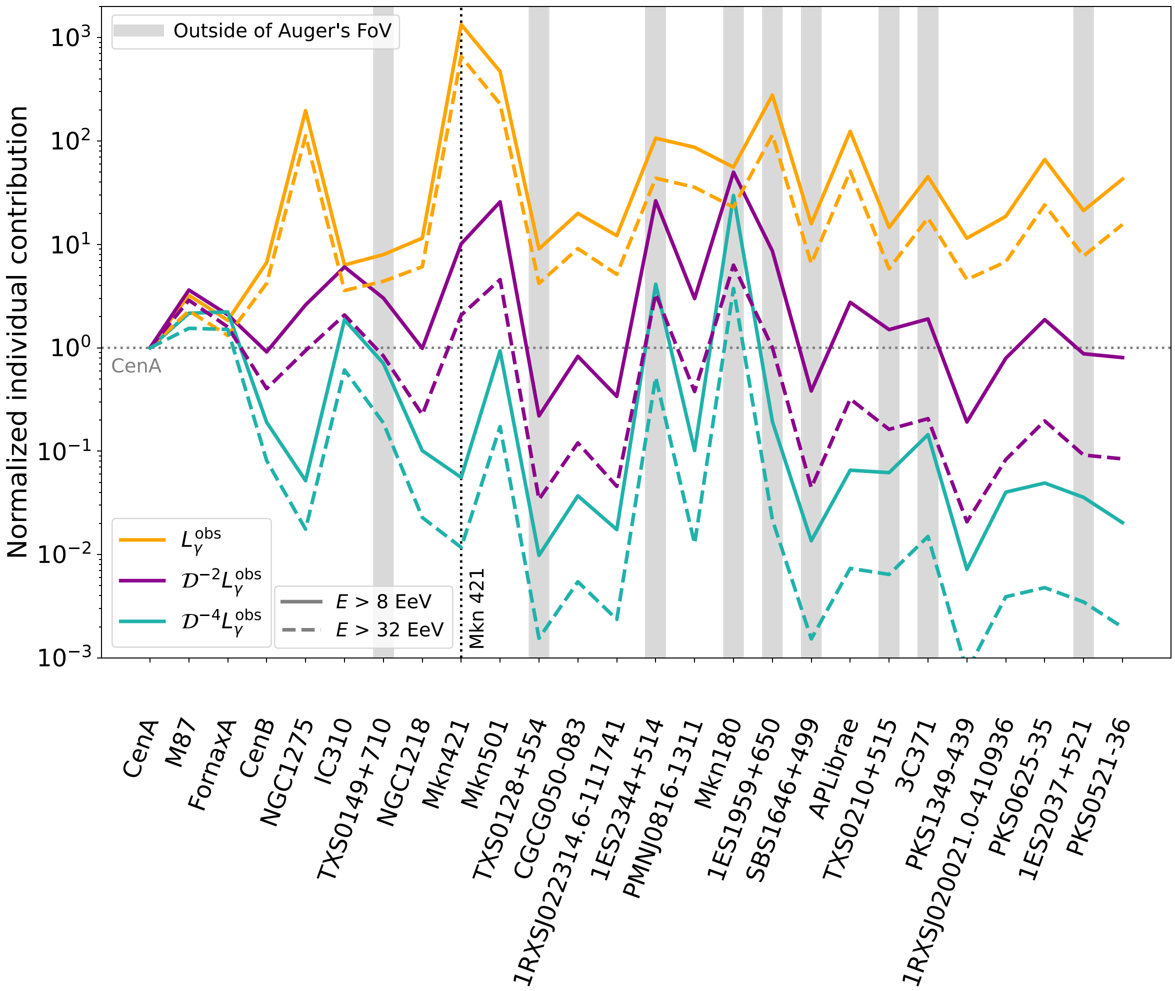

Figure 4. Relative contribution to the spectrum from each individual source. The contribution from Cen A is taken as the reference for each case. Different line colors show the different proxies considered in this work, while continuous and dashed lines show the contributions for energies above 8 and 32 EeV, respectively. Sources outside of the field of view of the Pierre Auger Observatory are highlighted by a gray band.

Table 1
Significance of the Tension of the Predicted Direction of the Dipole with Experimental Data

Field of View	Energy	$L_\gamma^{\rm obs}$	$\mathcal{D}^{-2}L_\gamma^{\rm obs}$	$\mathcal{D}^{-4}L_\gamma^{\rm obs}$
Auger	>8 EeV	5.9σ	4.9σ	3.5σ
	>32 EeV	2.1σ	2.0σ	1.1σ
Full sky	>8 EeV	8.7σ	9.8σ	8.7σ
	>32 EeV	1.5σ	1.7σ	1.2σ

$L_\gamma^{\rm int} = \mathcal{D}^{-q}L_\gamma^{\rm obs}$, with $q \sim 2$–4. This becomes highly relevant when different AGN classes are considered, such as blazars ($\mathcal{D} \sim 10$) and radio galaxies ($\mathcal{D} \sim 2$).

4. *Using intrinsic γ-ray luminosity or the radiative jet power as a UHECR proxy gives a better fit to the Pierre Auger Observatory data.* A combined fit of spectrum and composition data performs better when $L_\gamma^{\rm int}$ is considered. The spectral shape of local sources is changed due to an increase in the relative contribution of closer sources. For the simple combined fit proposed in this work, an improvement from $\chi^2/{\rm NDF} = 4.6$ to $\chi^2/{\rm NDF} = 3.1$ is found.
5. *Using intrinsic γ-ray luminosity or the radiative jet power as a UHECR proxy reconciles the arrival directions data.* The relative contribution of each source, particularly at the highest energies, is changed for different proxy assumptions. When $L_\gamma^{\rm int}$ is considered, the strong expected contribution from Mkn 421 vanishes. The predicted dipole shifts from 5.9 (2.1)σ up to 3.5 (1.1) σ away from the one measured by the Pierre Auger Observatory for $E > 8$ EeV ($>$ 32 EeV). The predicted hotspots also change significantly. For the new proxies proposed here, three main hotspots appear in locations similar to those of the two hotspots measured by the Pierre Auger Observatory and the hotspot measured by the Telescope Array Experiment.

The intrinsic γ-ray luminosity or the radiative jet power used here appears to be a better proxy than the observed γ-ray luminosity. Since the intrinsic γ-ray luminosity is related to the jet kinetic power (Y. Chen et al. 2023a), it agrees with authors who argue that the UHECR luminosity must scale with the jet power (B. Eichmann et al. 2018; J. H. Matthews & A. M. Taylor 2021). In particular, J. H. Matthews & A. M. Taylor (2021) suggests that radio luminosity is a better proxy for $L_{\rm CR}$, with reservations due to UHECR transport and the particular characteristics of different sources.

Our results resonate with other works that found AGN catalogs as promising source candidates (B. Eichmann et al.

2018; B. Eichmann 2019; B. Eichmann et al. 2022; C. de Oliveira & V. de Souza 2022, 2023). The contribution of the radio galaxies Cen A and For A have been proposed as responsible for the dipole and hotspots measured by the Pierre Auger Observatory (J. H. Matthews et al. 2018b; C. de Oliveira & V. de Souza 2022), and a powerful emission from Cen A and For A from past enhanced activity cannot be ruled out (J. H. Matthews et al. 2018b).

It is important to emphasize that since radio galaxies do not present a γ-ray signal enhanced by relativistic beaming, fewer of them are detectable with increasing distance when compared to blazars. This selection bias can underestimate the overall contribution of radio galaxies concerning blazars, especially when distant sources are considered.

In contrast to fully isotropic emission, J. P. Rachen & B. Eichmann (2019) propose that blazars could have an additional beamed UHECR emission. In this work, we neglect that based on the decollimation effect on the source region. Due to the energy dependence on the magnetic scattering of charged particles, the decollimation of a possible UHECR beam will also be energy dependent. We do not account for this effect here, and it will be addressed in future work.

After leaving the source, extragalactic and galactic magnetic fields also should decollimate an eventual residual UHECR beam. In this work, we follow the simplistic assumption of blurring the arrival directions due to a turbulent component of the extragalactic magnetic field. The regular component of the extragalactic magnetic field can cause amplification/suppression of sources and a shift of arrival directions, which can be significant even to nearby sources (R. G. Lang et al. 2021; C. de Oliveira & V. de Souza 2022, 2023) and must be taken into account in a detailed study. However, the extragalactic magnetic field structure seems to have a minor effect in the dipole direction for $E > 32$ EeV if the flux is dominated by nearby radio galaxies (C. de Oliveira & V. de Souza 2023). Deflections by the galactic magnetic field were not taken into account either. A detailed exploration of the effect of cosmic magnetic fields is beyond the scope of this study, since the extragalactic and galactic magnetic fields are complex and their effects on UHECRs are still open questions (A. Bakalová et al. 2023; D. Harari et al. 2002; S. Hackstein et al. 2018; C. de Oliveira & V. de Souza 2022).

Finally, the dominant sources of UHECRs can only be addressed by quantitative comparison of scenarios aiming at reproducing the energy spectrum, composition, and arrival directions. Other scenarios such as SBGs (especially due to the high rate of transient events, such as long γ-ray bursts; S. Marafico et al. 2024) and large-scale shocks in galaxy clusters and filaments (P. Simeon et al. 2023) remain as viable sources of UHECRs (M. Kachelriess 2022). The combined fit used in this work is a simplified version that does not take into account the full $X_{\max}$ distributions and the arrival direction distribution. Still, the results shown here for arrival direction maps and dipole indicate that a full fit with the proxies here proposed will decrease the tension with the data.

Therefore, even with the intrinsic limitations addressed above, the results of this work strengthen the hypothesis of AGNs as candidates for the origin of UHECRs, and provide the community with a more robust hypothesis about the proxies for $L_{\rm CR}$ using L_γ. In addition, it potentially reconciles the results using different proxies, since both the radio and the intrinsic γ-ray luminosity scale with the jet power. These assumptions could be used in future studies that aim to model the data or look for correlations in the arrival directions data from the Pierre Auger Observatory and the Telescope Array Experiment.

Acknowledgments

The idea for this work was developed during a series of two joint FAPESP/BAYLAT workshops titled "Astroparticle physics in the era of CTA and SWGO" at the Friedrich-Alexander-Universität Erlangen-Nürnberg and the Instituto de Física de São Carlos, Universidade de São Paulo in 2023 and 2024. We acknowledge the generous support for these workshops by FAPESP (through grant No. 2022/01271-7) and BAYLAT. The authors thank Vitor de Souza, James Matthews, and Teresa Bister for reading the paper and making useful comments. We thank the anonymous referee for a helpful report that improved the quality of this work. This study was financed, in part, by the São Paulo Research Foundation (FAPESP), Brasil, process numbers 2019/10151-2, 2020/15453-4, and 2021/01089-1. C.O. acknowledges the National Laboratory for Scientific Computing (LNCC/MCTI, Brazil) for providing HPC resources for the Santos Dumont supercomputer (http://sdumont.lncc.br).

Appendix
Doppler Factor Estimations

The energy flux integrated from 10 GeV to 1 TeV (erg cm^{-2} s^{-1}),

$$S_\gamma^{0.01-1\ \rm TeV} = \int_{10\ \rm GeV}^{1\ \rm TeV} E\frac{dN}{dE}dE, \tag{A1}$$

measured by the Fermi-LAT satellite, was used to weigh the UHECR flux from each source. The isotropic γ-ray luminosity is estimated as

$$L_{0.01-1\ \rm TeV}^{\rm iso} = 4\pi d^2 S_\gamma^{0.01-1\ \rm TeV}, \tag{A2}$$

where S_γ is the γ-ray energy flux and d is the distance, found in the Auger catalog (A. Abdul Halim et al. 2024), and the redshift dependence is omitted since the most distant source is PKS0521-36, at $d \approx 241$ Mpc, whose $z \approx 0.056 \ll 1$.

The intrinsic and observed luminosities are related by the Doppler factor ($\mathcal{D}$) of the plasma in the jet by

$$L^{\rm int} = \mathcal{D}^q L^{\rm iso}, \tag{A3}$$

where $q = -2$ or -4 (see Section 3.1).

Obtaining reliable estimations of the viewing angle and bulk velocities is challenging, with different indirect methods proposed in the literature. These methods do not always agree (I. Liodakis et al. 2017). I. Liodakis et al. (2018) obtained $\mathcal{D}$ based on the observed and equipartition brightness temperature of flares. L. Zhang et al. (2020) determined $\mathcal{D}$ from correlations between the γ-ray luminosity and broad-line luminosity, and claim that the results from this method are consistent with that of I. Liodakis et al. (2018). X.-H. Ye et al. (2023) combined the results from I. Liodakis et al. (2018) and L. Zhang et al. (2020) with the Fermi-LAT data for BL Lacs to estimate the Doppler factor of FR I radio galaxies within a unification scenario.

The data from L. Zhang et al. (2020) and X.-H. Ye et al. (2023) were combined with L. Chen (2018), and provide a Doppler factor of 15 among the 26 objects found in the Auger catalog (Table 2). To get the data for the remaining objects, we use the empirical relationship between $f_b \approx \mathcal{D}^{-2}$ and the

Table 2
Relevant Data for the AGNs Used in the Analysis

AGN[a]	Class	(R.A., Decl.)[b]	Distance (Mpc)	$F_{3fgl}/10^{-11}$[c]	$F_{3fhl}/10^{-12}$[d]	$\mathcal{D}$	Ref.[e]	$\mathcal{D}^{-2}F_{3fhl}/10^{-12}$	$\mathcal{D}^{-4}F_{3fhl}/10^{-12}$
Cen A	RG	(201.37, −43.02)	3.68	5.86	7.41	1.0	Y23	7.41	7.41
M87	RG	(187.71, 12.39)	16.7	1.64	9.55	1.3	Y23	5.40	3.05
For A	RG	(50.67, −37.21)	20.4	0.61	2.59	1.0	Y23	2.59	2.59
Cen B	RG	(206.7, −60.41)	55.2	2.04	2.12	2.3	Y23	0.40	7.59×10^{-2}
NGC1275	RG	(49.95, 41.51)	78.0	29.13	47.97	7.5	Y23	0.86	1.52×10^{-2}
IC 310	RG	(49.18, 41.32)	83.2	0.33	6.90	1.9	Y23	1.89	0.52
TXS0149+710	BCU	(28.36, 71.25)	103.3	0.25	3.72	2.2	Y23	0.76	0.16
NGC1218	RG	(47.11, 4.11)	124.7	0.93	2.42	3.4	Y23	0.22	1.90×10^{-2}
Mkn 421	BLL	(166.1, 38.21)	133.7	40.44	437.47	14.5	Z20	2.08	0.99×10^{-2}
Mkn 501	BLL	(253.47, 39.76)	152.1	11.77	156.19	5.7	Z20	4.84	0.15
TXS0128+554	BCU	(22.81, 55.75)	162.9	0.61	0.99	5.1	C23	0.38×10^{-1}	0.14×10^{-2}
CGCG050-083	BCU	(235.89, 4.87)	178.6	0.51	3.60	5.1	C23	0.14	0.52×10^{-2}
1RXSJ022314.6-111741	BLL	(35.81, −11.29)	182.8	0.26	1.24	4.8	C23	0.54×10^{-1}	0.23×10^{-2}
1ES2344+514	BLL	(356.76, 51.69)	196.8	3.17	30.74	2.7	C18	4.22	0.57
PMNJ0816-1311	BLL	(124.11, −13.2)	200.4	1.60	16.07	5.9	C23	0.46	1.30×10^{-2}
Mkn 180	BLL	(174.11, 70.16)	203.2	1.25	15.25	1.4	C18	7.78	3.97
1ES1959+650	BLL	(299.97, 65.16)	211.8	10.50	67.74	7.3	C23	1.27	2.37×10^{-2}
SBS1646+499	BLL	(251.9, 49.83)	212.8	1.45	1.89	5.8	C18	0.56×10^{-1}	0.17×10^{-2}
AP Librae	BLL	(229.42, −24.37)	216.8	7.53	20.33	7.1	C23	0.40×10^{-1}	0.80×10^{-2}
TXS0210+515	BLL	(33.55, 51.77)	218.8	0.54	6.21	5.4	C23	0.21	0.73×10^{-2}
3C371	BLL	(271.71, 69.82)	225.9	3.29	4.29	4.0	Z20	0.27	1.71×10^{-2}
PKS1349-439	BLL	(208.24, −44.21)	228.0	0.80	0.87	5.7	C23	0.27×10^{-1}	0.08×10^{-2}
1RXSJ020021.0-410936	BLL	(30.09, −41.16)	234.4	0.20	2.72	4.9	C23	0.11	0.46×10^{-2}
PKS0625-35	BLL	(96.78, −35.49)	238.8	1.54	12.38	6.8	Y23	0.26	0.56×10^{-2}
1ES2037+521	BLL	(309.85, 52.33)	238.8	0.55	3.72	5.5	C23	0.12	0.41×10^{-2}
PKS0521-36	BLL	(80.76, −36.46)	241.0	5.25	5.52	7.0	C23	0.11	0.23×10^{-2}

Notes.
[a] Associated source found in the Fermi-LAT catalog.
[b] Equatorial coordinates, in degrees.
[c] Energy flux from the Fermi 3FGL-DR4 catalog (0.1–100 GeV), in erg per square centimeter per second (https://heasarc.gsfc.nasa.gov/W3Browse/fermi/fermi3fgl.html).
[d] Energy flux from the Fermi 3FHL catalog (10 GeV–1 TeV), in erg per square centimeter per second (https://heasarc.gsfc.nasa.gov/W3Browse/fermi/fermi3fhl.html).
[e] **References.** C18 = L. Chen (2018), Z20 = L. Zhang et al. (2020), Y23 = X.-H. Ye et al. (2023), C23 = fit from Y. Chen et al. (2023a).

observed luminosity $L^{\rm iso}$,

$$\log f_b = (-0.21 \pm 0.03)\log L^{\rm iso} + (7.67 \pm 1.54), \qquad (A4)$$

found by Y. Chen et al. (2023a) using the data from I. Liodakis et al. (2018) for FSRQs, BLLs, γNLS1s, and radio galaxies. This expression uses $L^{\rm iso}$ calculated from the Fermi 4FGL-DR4 catalog, between 0.1 and 100 GeV, while we are using the 4FHL catalog to weight the UHECR flux.

ORCID iDs

Cainã de Oliveira https://orcid.org/0000-0003-4038-1509
Rodrigo Guedes Lang https://orcid.org/0000-0003-0492-5628
Pedro Batista https://orcid.org/0000-0001-8138-1391

References

Aab, A., Abreu, P., Aglietta, M., et al. 2014, PhRvD, 90, 122005
Aab, A., Abreu, P., Aglietta, M., et al. 2017, JCAP, 2017, 038
Aab, A., Abreu, P., Aglietta, M., et al. 2018, ApJL, 853, L29
Abbasi, R. U., Abe, M., Abu-Zayyad, T., et al. 2018, ApJL, 867, L27
Abdul Halim, A., Abreu, P., Aglietta, M., et al. 2023, ICRC (Nagoya), 38, 252
Abdul Halim, A., Abreu, P., Aglietta, M., et al. 2023, ICRC (Nagoya), 38, 521
Abdul Halim, A., Abreu, P., Aglietta, M., et al. 2024, ApJ, 976, 48
Abdul Halim, A., Abreu, P., Aglietta, M., et al. 2024, JCAP, 2024, 022
Abdul Halim, A., Abreu, P., Aglietta, M., et al. 2024, JCAP, 2024, 094
Abreu, P., Aglietta, M., Albury, J. M., et al. 2022, ApJ, 935, 170
Abu-Zayyad, T., Aida, R., Allen, M., et al. 2012, NIMPA, 689, 87
Adebahr, B., Brienza, M., & Morganti, R. 2019, A&A, 622, A209
Ajello, M., Atwood, W. B., Baldini, L., et al. 2017, ApJS, 232, 18
Aloisio, R., Boncioli, D., di Matteo, A., et al. 2017, JCAP, 2017, 009
Alves Batista, R., Biteau, J., Bustamante, M., et al. 2019, FrASS, 6, 23
Alves Batista, R., Dundovic, A., Erdmann, M., et al. 2016, JCAP, 2016, 038
Andati, L. A. L., Baidoo, L. M., Ramaila, A. J. T., et al. 2024, MNRAS, 529, 1626
Araudo, A. T., Bell, A. R., Blundell, K. M., & Matthews, J. H. 2017, MNRAS, 473, 3500
Atoyan, A., & Dermer, C. 2004, NewAR, 48, 381
Bakalová, A., Vcha, J., & Trvncek, P. 2023, JCAP, 2023, 016
Begelman, M. C., & Cioffi, D. F. 1989, ApJL, 345, L21
Bell, A. R., Araudo, A. T., Matthews, J. H., & Blundell, K. M. 2017, MNRAS, 473, 2364
Blandford, R., Meier, D., & Readhead, A. 2019, ARA&A, 57, 467
Böttcher, M. 2012, in Relativistic Jets from Active Galactic Nuclei, ed. M. Böttcher, D. E. Harris, & H. Krawczynski (Berlin: Wiley)
Böttcher, M., Reimer, A., Sweeney, K., & Prakash, A. 2013, ApJ, 768, 54
Cao, G., & Wang, J. 2014, ApJ, 783, 108
Carilli, C., & Barthel, P. 1996, A&ARv, 7, 1
Cerutti, B., & Giacinti, G. 2023, A&A, 676, A23
Chen, L. 2018, ApJS, 235, 39
Chen, Y., Gu, Q., Fan, J., et al. 2023a, MNRAS, 519, 6199
Chen, Y., Gu, Q., Fan, J., et al. 2023b, ApJS, 265, 60
Coimbra-Araújo, C. H., & Anjos, Q. 2020, CQGra, 38, 015007
Coimbra-Arajo, C. H., & dos Anjos, R. C. 2022, Galax, 10, 84
Condorelli, A., Biteau, J., & Adam, R. 2023, ApJ, 957, 80
De Angelis, A., Galanti, G., & Roncadelli, M. 2013, MNRAS, 432, 3245
de Oliveira, C., & de Souza, V. 2022, ApJ, 925, 42

de Oliveira, C., & de Souza, V. 2023, JCAP, 2023, 058
de Oliveira, C. A., Maia, L. P., & de Souza, V. 2024, JCAP, 04, 043
Dermer, C. D., & Menon, G. 2009, High Energy Radiation from Black Holes: Gamma Rays, Cosmic Rays, and Neutrinos (Princeton, NJ: Princeton Univ. Press)
di Matteo, A., Anchordoqui, L., Bister, T., et al. 2023, EPJ Web Conf., 283, 03002
Dubey, R. P., Fendt, C., & Vaidya, B. 2023, ApJ, 952, 1
Eichmann, B. 2019, JCAP, 2019, 009
Eichmann, B., Kachelrie, M., & Oikonomou, F. 2022, JCAP, 2022, 006
Eichmann, B., Rachen, J., Merten, L., van Vliet, A., & Tjus, J. B. 2018, JCAP, 2018, 036
Finke, J. D., Dermer, C. D., & Bttcher, M. 2008, ApJ, 686, 181
Fisher, R. 1953, RSPSA, 217, 295
Gilmore, R. C., Somerville, R. S., Primack, J. R., & Domnguez, A. 2012, MNRAS, 422, 3189
Globus, N., Allard, D., & Parizot, E. 2008, A&A, 479, 97
Goodger, J. L., Hardcastle, M. J., Croston, J. H., et al. 2009, ApJ, 708, 675
Gréaux, L., Biteau, J., & Nievas Rosillo, M. 2024, ApJL, 975, L18
Guidetti, D., Laing, R. A., Bridle, A. H., Parma, P., & Gregorini, L. 2011, MNRAS, 413, 2525
Hackstein, S., Vazza, F., Brüggen, M., Sorce, J. G., & Gottlöber, S. 2018, MNRAS, 475, 2519
Harari, D., Mollerach, S., Roulet, E., & Sánchez, F. 2002, JHEP, 2002, 045
Hardcastle, M. J., Croston, J. H., & Kraft, R. P. 2007, ApJ, 669, 893
Hardcastle, M. J., & Krause, M. G. H. 2014, MNRAS, 443, 1482
Hardcastle, M. J., Lenc, E., Birkinshaw, M., et al. 2015, MNRAS, 455, 3526
Harvey, A. L. W., Georganopoulos, M., & Meyer, E. T. 2020, NatCo, 11, 5475
Hillas, A. M. 1984, ARA&A, 22, 425
Kachelriess, M. 2022, ICRC (Berlin), 37, 18
Katsoulakos, G., & Rieger, F. M. 2018, ApJ, 852, 112
Kelner, S. R., Aharonian, F. A., & Bugayov, V. V. 2006, PhRvD, 74, 034018
Kim, J., Ivanov, D., Kawata, K., Sagawa, H., & Thomson, G. 2023, ICRC (Nagoya), 38, 244
Kimura, S. S., Murase, K., & Zhang, B. T. 2018, PhRvD, 97, 023026
Kotera, K., & Olinto, A. V. 2011, ARA&A, 49, 119
Lang, R. G., Taylor, A. M., Ahlers, M., & de Souza, V. 2020, PhRvD, 102, 063012
Lang, R. G., Taylor, A. M., & de Souza, V. 2021, PhRvD, 103, 063005
Lemoine, M., & Pelletier, G. 2010, MNRAS, 402, 321
Linsley, J. 1963, PhRvL, 10, 146
Liodakis, I., Hovatta, T., Huppenkothen, D., et al. 2018, ApJ, 866, 137
Liodakis, I., Marchili, N., Angelakis, E., et al. 2017, MNRAS, 466, 4625
Marafico, S., Biteau, J., Condorelli, A., Deligny, O., & Bregeon, J. 2024, ApJ, 972, 4
Maraschi, L., & Tavecchio, F. 2003, ApJ, 593, 667
Massaro, F., & Ajello, M. 2011, ApJL, 729, L12
Matthews, J. H., Bell, A. R., & Blundell, K. M. 2020, NewAR, 89, 101543
Matthews, J. H., Bell, A. R., Blundell, K. M., & Araudo, A. T. 2018a, MNRAS, 482, 4303
Matthews, J. H., Bell, A. R., Blundell, K. M., & Araudo, A. T. 2018b, MNRAS, 479, L76
Matthews, J. H., & Taylor, A. M. 2021, MNRAS, 503, 5948
Mattia, G., Del Zanna, L., Bugli, M., et al. 2023, A&A, 679, A49
Mattia, G., & Caprioli, D. 2019, ApJ, 679, 8
Medina-Torrejón, T. E., de Gouveia Dal Pino, E. M., Kadowaki, L. H. S., et al. 2021, ApJ, 908, 193
Morganti, R. 2017, FrASS, 4, 42
Nagano, M., & Watson, A. A. 2000, RvMP, 72, 689
Nemmen, R. S., Georganopoulos, M., Guiriec, S., et al. 2012, Sci, 338, 1445
O'Sullivan, S., Reville, B., & Taylor, A. M. 2009, MNRAS, 400, 248
Partenheimer, A., Fang, K., Batista, R. A., & de Almeida, R. M. 2024, ApJL, 967, L15
Pierog, T., Karpenko, I., Katzy, J. M., Yatsenko, E., & Werner, K. 2015, PhRvC, 92, 034906
Rachen, J. P., & Eichmann, B. 2019, ICRC (Madison, WI), 36, 396
Reville, B., & Bell, A. R. 2014, MNRAS, 439, 2050
Rieger, F. M. 2022, Univ, 8, 607
Rodrigues, X., Fedynitch, A., Gao, S., Boncioli, D., & Winter, W. 2018, ApJ, 854, 54
Seo, J., Ryu, D., & Kang, H. 2023, ApJ, 944, 199
Seo, J., Ryu, D., & Kang, H. 2024, ApJ, 962, 46
Shukla, A., & Mannheim, K. 2020, NatCo, 11, 4176
Simeon, P., Globus, N., Barrow, K., & Blandford, R. D. 2023, ICRC (Nagoya), 38, 369
Snios, B., Johnson, A. C., Nulsen, P. E. J., et al. 2020, ApJ, 891, 173
Sun, X.-n., Yang, R.-z., Mckinley, B., & Aharonian, F. 2016, A&A, 595, A29
The Pierre Auger Collaboration 2015, NIMPA, 798, 172
Turner, R. J., Yates-Jones, P. M., Shabala, S. S., Quici, B., & Stewart, G. S. C. 2022, MNRAS, 518, 945
Verzi, V. 2020, ICRC (Madison, WI), 36, 450
Wykes, S., Hardcastle, M. J., & Croston, J. H. 2015, MNRAS, 454, 3277
Wykes, S., Intema, H. T., Hardcastle, M. J., et al. 2014, MNRAS, 442, 2867
Ye, X.-H., Zeng, X.-T., Huang, D.-Y., et al. 2023, PASP, 135, 014101
Yushkov, A. 2020, ICRC (Madison, WI), 36, 482
Zech, A., & Lemoine, M. 2021, A&A, 654, A96
Zhang, B. T., & Murase, K. 2023, MNRAS, 524, 76
Zhang, L., Chen, S., Xiao, H., Cai, J., & Fan, J. 2020, ApJ, 897, 10